

# A numerical study of nonlinear infrasound propagation in a windy atmosphere

R. Sabatini,<sup>a)</sup> O. Marsden, C. Bailly, and C. Bogey

*Laboratoire de Mécanique des Fluides et d'Acoustique, Unité Mixte de Recherche CNRS 5509, École Centrale de Lyon, Université de Lyon, 69134 Écully Cedex, France*

(Received 11 December 2015; revised 16 June 2016; accepted 5 July 2016; published online 27 July 2016)

Direct numerical simulations of the two-dimensional unsteady compressible Navier-Stokes equations are performed to study the acoustic field generated by an infrasonic source in a realistic atmosphere. Some of the main phenomena affecting the propagation of infrasonic waves at large distances from the source are investigated. The effects of thermal and wind-related refraction on the signals recorded at ground level are highlighted, with particular emphasis on the phase shift induced by the presence of caustics in the acoustic field. Nonlinear waveform steepening associated with harmonic generation, and period lengthening, both of which are typical of large source amplitudes, are illustrated, and the importance of thermoviscous absorption in the upper atmosphere is clearly demonstrated. The role of diffraction in the shadow zone, around caustics and at stratospheric altitudes is also pointed out. The Navier-Stokes equations are solved using high-order finite-differences and a Runge-Kutta time integration method both originally developed for aeroacoustic applications, along with an adaptive shock-capturing algorithm which allows high-intensity acoustic fields to be examined. An improvement to the shock detection procedure is also proposed in order to meet the specificities of nonlinear propagation at long range. The modeling as well as the numerical results are reported in detail and discussed. © 2016 Acoustical Society of America. [<http://dx.doi.org/10.1121/1.4958998>]

[MDV]

Pages: 641–656

## I. INTRODUCTION

Infrasonic waves can be generated in the atmosphere by natural events, such as volcanic eruptions, earthquakes, and meteors, or by man-made sources, like explosions or supersonic flights. These waves can propagate over thousands of kilometers through the Earth's atmosphere and can potentially carry relevant information about their source. Accordingly, a worldwide infrasound monitoring network has been developed<sup>1,2</sup> to verify compliance with the Comprehensive Nuclear-Test-Ban Treaty (CTBT), which prohibits all types of nuclear detonation. At the date of writing the present paper, the network consists of about 48 certified ground stations, that record pressure fluctuations of frequency lower than 4 Hz. Infrasound monitoring can also be used in the field of atmospheric tomography,<sup>3</sup> for instance, to study gravity waves.<sup>4</sup>

The determination of the nature of infrasound sources as well as their spatial location, based on pressure signals recorded by the CTBT stations, depends on the ability to simulate long-range atmospheric propagation in a time-accurate manner. While a preliminary analysis of the acoustic field can be carried out by techniques accounting only for refraction effects induced by both temperature and wind speed gradients,<sup>5</sup> the computation of an accurate acoustic time signature requires the integration of nonlinear distortion<sup>6–8</sup> and thermoviscous atmospheric absorption<sup>9</sup> among other phenomena. More specifically, the exponential reduction with altitude

of the mean atmospheric density tends to amplify nonlinearities, which lead to signal steepening and lengthening. Thermoviscous absorption also increases as the mean atmospheric density diminishes, due to the increase of the mean kinematic viscosity. Furthermore, a caustic is generally observed in the thermosphere.<sup>6</sup> Signals detected at barometric stations located in the audibility zone of the caustic are strongly affected. In particular, a phase shift is induced by the caustic,<sup>10</sup> so that for an incoming N-like wave, typical for instance of explosive phenomena, a U-shaped signature is observed at ground level.<sup>6,11,12</sup>

Numerical approaches for atmospheric infrasonic propagation studies have naturally been based on simplified equations. Ray tracing,<sup>7,8,13</sup> parabolic models<sup>14</sup> or the normal mode theory have been the most commonly used techniques.<sup>15</sup> Their efficiency in terms of computational time is however obtained at the expense of generality and some of the aforementioned phenomena are inherently excluded by these approaches. Over the past decade, progress has been made toward the simulation of acoustic propagation by directly solving the fluid dynamics equations. One of the first numerical investigations was carried out by Wochner *et al.*<sup>16</sup> to analyze a realistic absorption model accounting for molecular relaxation. Currently, most numerical simulations are performed in two dimensions,<sup>17–19</sup> but a proof of concept computation in three dimensions, based on simplified linearized Euler equations, was performed by Del Pino *et al.*<sup>20</sup> A complete Navier-Stokes modeling in an axisymmetric cylindrical coordinate system was proposed by de Groot-Hedlin,<sup>21</sup> with some example calculations of infrasound propagation at short range. Understandably, progress

<sup>a)</sup>Also at Commissariat à l'Énergie Atomique et aux Énergies Alternatives, Direction des Applications Militaires, Île de France, 91297 Arpajon, France. Electronic mail: roberto.sabatini@doctorant.ec-lyon.fr

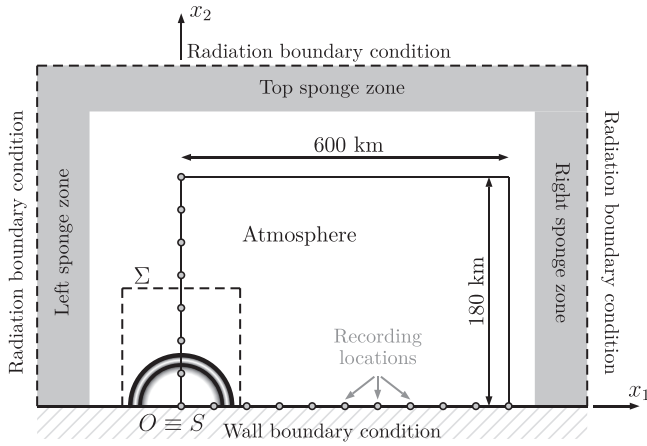


FIG. 1. Sketch of the computational domain. The source is located at the origin  $O \equiv S$ , and the inner black rectangle indicates the physical domain.

in the direct simulation of the fluid dynamics equations is expected to lead to better interpretation of experimental observations and improved physical modeling of infrasonic waves. However, as also highlighted by the previous authors, numerical accuracy is an essential requirement, in particular, for the computation of the nonlinear propagation of infrasonic signals over very large distances. In a recent work of Marsden *et al.*,<sup>22</sup> the feasibility of using numerical simulation of the Navier-Stokes equations for the detailed description of long-range infrasound propagation in the atmosphere was analyzed. In particular, a first investigation of the sound field generated by an infrasonic source of main frequency of 0.1 Hz in a realistic atmosphere at rest was computed using a high-order finite-difference time-domain (FDTD) method originally developed for aeroacoustic applications.<sup>23–25</sup> The numerical schemes,<sup>26–28</sup> designed to minimize the numerical dispersion and dissipation errors, were shown to be well suited for the simulation of nonlinear acoustic propagation over very large distances.

In the present work, numerical simulations of the two-dimensional Navier-Stokes equations are carried out for four different configurations in order to investigate some of the main physical phenomena affecting acoustic signals recorded at long range, namely, refraction due to the temperature gradient, refraction due to the wind profile, thermoviscous absorption, nonlinear waveform modifications and diffraction. The aim is not to provide direct comparisons with experiments, as undertaken in Gainville *et al.*,<sup>29</sup> for instance, which is precluded by the two-dimensional nature of this study, but rather to highlight some specific physical features of infrasonic waves propagating in the Earth's atmosphere. In each case, the atmospheric propagation of a finite-duration signal emitted from an infrasonic source of frequency of 0.1 Hz and placed at ground level is computed. The realistic atmosphere specification includes the definition of range-independent vertical temperature and wind profiles, which follow the main trends observed during the *Misty Picture experiment* from the ground up to an altitude of 180 km.<sup>29,30</sup> The physical domain of interest spans 600 km in the horizontal direction and 180 km the vertical direction. The infrasonic source is implemented as a forcing term in the energy equation. The

two-dimensional Navier-Stokes equations are solved on a regular Cartesian grid with the explicit finite-difference time-domain (FDTD) algorithm employed in the earlier work of Marsden *et al.*<sup>22</sup> Spatial discretization is performed with a low-dissipation and low-dispersion optimized 11-point stencil scheme, while time integration is carried out thanks to a six-step second-order optimized low-storage Runge-Kutta algorithm.<sup>26,27</sup> In order to handle the acoustic shocks which are generated during the propagation of large-amplitude signals, the shock-capturing technique proposed by Bogey *et al.*<sup>28</sup> is used. The methodology consists in applying artificial dissipation only where necessary, i.e., only near shock fronts, in such a way that smooth regions of the solution are not affected. Clearly, the efficacy of the method strongly depends on

TABLE I. Spline coefficients for the speed of sound and the wind.

$x_2$ (km)	$\bar{c}$ (m s <sup>-1</sup> )	$\bar{c}''$ (m km <sup>-2</sup> s <sup>-1</sup> )
0	340	-1.2000000000
10	300	+ 0.7040957867
20	290	+ 0.1836168532
50	330	-0.2576768707
70	290	+ 0.0129590737
90	265	+ 0.4308405759
120	425	-0.1281079686
160	580	-0.0935025416
180	600	-0.0452688129
250	550	-0.0038182448
300	480	-0.0005818014
350	410	+ 0.0061454503
400	350	+ 0.0000000000
$x_2$ (km)	$\bar{u}_1$ (m s <sup>-1</sup> )	$\bar{u}_1''$ (m km <sup>-2</sup> s <sup>-1</sup> )
0	+ 00.0	+ 0.0000000000
10	+ 04.6	-0.4234911283
15	-00.3	+ 0.8129467697
20	+ 04.7	-0.4522959507
30	+ 02.6	+ 0.2244144671
40	+ 07.4	-0.0313619178
50	+ 21.5	+ 0.4590332040
55	+ 30.6	-2.1994753882
60	+ 09.7	+ 1.1388683490
65	+ 10.2	+ 2.7800019922
70	+ 49.8	-2.8748763180
80	+ 16.7	+ 0.4966279578
95	-21.8	+ 0.5584910193
110	+ 28.2	-0.3705920349
125	+ 38.6	-0.1321228796
140	+ 21.0	+ 0.1524168868
160	+ 22.6	-0.0583669442
180	+ 20.0	+ 0.0180508898
200	+ 18.0	-0.0048366151
220	+ 16.0	+ 0.0012955706
240	+ 14.0	-0.0003456673
260	+ 12.0	+ 0.0000870984
280	+ 10.0	-0.0000027265
300	+ 08.0	-0.0000761925
320	+ 06.0	+ 0.0003074966
340	+ 04.0	-0.0011537937
360	+ 02.0	+ 0.0043076783
380	+ 01.0	-0.0010769196
400	+ 00.0	+ 0.0000000000

the ability to identify the presence of discontinuities. To this end, a new shock sensor based on the smoothness indicators first proposed for the weighted essentially non-oscillatory schemes<sup>31,32</sup> is also developed in this work. The entire algorithm is implemented in OpenCL and runs on a AMD R290 Graphic Processing Unit (GPU), allowing very high computational performance to be achieved.<sup>22</sup>

The paper is organized as follows. The present numerical modeling of long-range atmospheric infrasound propagation is presented in Sec. II. The computational domain and the atmospheric mean flow are first defined. The set of governing equations and the infrasonic source are then described and a detailed illustration of the numerical method is given. The results obtained for the four configurations are reported in Sec. III. Time signals at various altitudes and at ground level are examined and the aforementioned physical aspects are discussed. Concluding remarks are finally drawn in Sec. IV.

## II. NUMERICAL MODELING OF LONG-RANGE ATMOSPHERIC INFRASOUND PROPAGATION

### A. Computational domain

The present studies involve computing the two-dimensional acoustic field generated by a source of infrasound in a realistic atmosphere up to 180 km altitude and 600 km range. A sketch of the computational domain is given in Fig. 1. A Cartesian coordinate system  $Ox_1x_2$  with its origin at ground level is used. The Earth's surface is modeled as a perfectly reflecting flat wall and the atmosphere, as a vertically stratified medium. The infrasonic source  $S$  is placed at the origin of the domain. The physical domain of  $[0, 600]$  km  $\times$   $[0, 180]$  km is surrounded by sponge zones in order for outgoing waves to leave the computational domain without appreciable reflections.

### B. Atmospheric mean flow

For the purpose of the present investigations, air in the atmosphere is assumed to behave as a single ideal gas satisfying the equation of state  $p = \rho r T$ , where  $p$  is the pressure,  $\rho$  the fluid density,  $T$  the temperature and  $r$  the specific gas constant. The atmosphere is defined as a vertically-stratified and range-invariant medium, constructed from a spline-based profile of sound speed  $\bar{c}(x_2)$  which reproduces the large scales observed

during the *Misty Picture experiment*<sup>29</sup> from 0 km to around 180 km. Spline knot locations and values are taken from a previous study,<sup>30</sup> with additional knots specified to allow the profile to be defined throughout the entire computational domain. They are provided in Table I and discussed in Appendix A. The resulting profile is illustrated in Fig. 2(a), along with a synthetic nomenclature of the different atmospheric layers.

The mean temperature  $\bar{T}(x_2)$  is computed from the speed of sound according to  $\bar{T}(x_2) = \bar{c}(x_2)^2 / (\gamma r)$ , where  $\gamma$  represents the ratio of specific heats, while pressure  $\bar{p}(x_2)$  is obtained by solving the hydrostatic equilibrium condition

$$\frac{d\bar{p}}{dx_2} = -\bar{\rho}g = -\frac{g}{r\bar{T}}\bar{p}, \quad (1)$$

where  $g$  is the gravitational acceleration, here considered to be independent of altitude. Equation (1) is integrated numerically from  $x_2 = 0$  km with the ground-level pressure fixed to  $\bar{p}_g = 10^5$  Pa. Finally, the density profile  $\bar{\rho}$  is determined from the equation of state  $\bar{\rho} = \bar{p} / (r\bar{T})$ . Mean pressure and density vertical profiles are shown in Fig. 2(c).

To complete the construction of the mean atmospheric state, a horizontal wind  $\bar{\mathbf{u}} = (\bar{u}_1(x_2), \bar{u}_2 \equiv 0)$  is specified by a spline-based profile  $\bar{u}_1(x_2)$  derived from data observed during the *Misty Picture experiment* in the East-West direction. The spline values are reported in Table I and the wind profile is shown in Fig. 2(b). Strong wind gradients are clearly visible in the stratosphere and mesosphere.

### C. Governing equations

Sound propagation is governed by the two-dimensional compressible Navier-Stokes equations, which can be written as

$$\begin{aligned} \frac{\partial \rho}{\partial t} + \frac{\partial(\rho u_j)}{\partial x_j} &= 0, \\ \frac{\partial(\rho u_i)}{\partial t} + \frac{\partial(\rho u_i u_j)}{\partial x_j} &= -\frac{\partial p'}{\partial x_i} + \frac{\partial \tau'_{ij}}{\partial x_j} - \rho' g \delta_{i2}, \\ \frac{\partial(\rho e_i)}{\partial t} + \frac{\partial(\rho e_i u_j)}{\partial x_j} &= -\frac{\partial(p' u_j)}{\partial x_j} - \bar{p} \frac{\partial u_j}{\partial x_j} - \frac{\partial q'_j}{\partial x_j} \\ &\quad + \frac{\partial(u_i \tau'_{ij})}{\partial x_j} - \rho' g u_2 + \Lambda_s, \end{aligned} \quad (2)$$

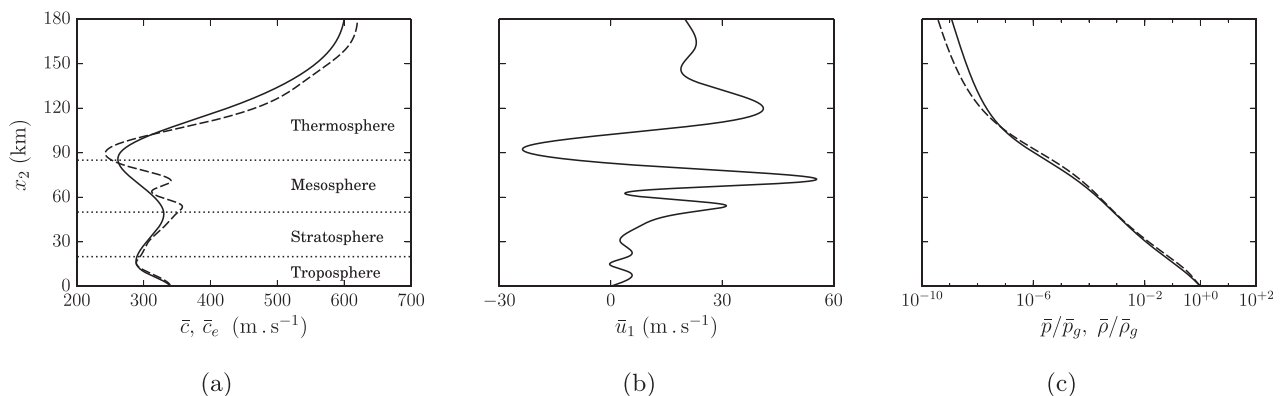


FIG. 2. (a) Atmospheric speed of sound  $\bar{c}$  (solid line) and effective celerity  $\bar{c}_e = \bar{c} + \bar{u}_1$  (dashed line) profiles; (b) wind profile  $\bar{u}_1$ ; (c) atmospheric pressure  $\bar{p}$  (solid line) and density  $\bar{\rho}$  (dashed line) profiles normalized with respect to their values at ground level.

where  $u_i$  is the velocity component in the  $i$ th direction,  $p' = p - \bar{p}$  the pressure perturbation,  $\rho' = \rho - \bar{\rho}$  that of density,  $e_t$  the total energy per unit mass,  $\tau'_{ij}$  the viscous stress tensor,  $q'_i$  the heat flux and  $\Lambda_s$  the source forcing term. Note that, following Marsden *et al.*,<sup>22</sup> the hydrostatic equilibrium condition  $d\bar{p}/dx_2 = -\bar{\rho}g$  is here subtracted from the classical Navier-Stokes system in order to avoid its high-precision computation at each time step. Moreover, because of the non-vanishing terms  $\partial\bar{\tau}_{12}/\partial x_1$  and  $\partial\bar{q}_2/\partial x_2$ , the initial mean atmosphere is not fully consistent with the Navier-Stokes equations and thus tends to evolve in time. To take into account this issue, the numerical solution is computed by neglecting the diffusion of the mean flow during the acoustic propagation. The viscous and thermal terms are thus calculated using the perturbed variables  $u'_i = u_i - \bar{u}_i$  and  $T' = T - \bar{T}$ . More specifically, the viscous stress tensor and the heat flux are computed, respectively, as

$$\tau'_{ij} = \mu \left( \frac{\partial u'_i}{\partial x_j} + \frac{\partial u'_j}{\partial x_i} - \frac{2}{3} \frac{\partial u'_k}{\partial x_k} \delta_{ij} \right) \quad (3)$$

$$\Lambda_s(x_1, x_2, t) = \frac{\mathcal{A}_s}{2} \begin{cases} \sin(\omega_s t) [1 - \cos(\omega_s t)] e^{-\log(2)(x_1^2 + x_2^2)/b_s^2} & t \in [0, T_s] \\ 0 & \text{otherwise.} \end{cases} \quad (6)$$

The parameter  $\mathcal{A}_s$ , expressed in  $\text{J m}^{-3} \text{s}^{-1}$ , is used to adjust the source strength. The Gaussian half-width of the source is set to  $b_s = 600 \text{ m}$  and the central frequency to  $f_s = \omega_s / (2\pi) = 1/T_s = 0.1 \text{ Hz}$ . The total emission duration is thus  $T_s = 10 \text{ s}$ . The temporal evolution of  $\Lambda_s$  is chosen in order to generate a N-like pressure signature at the source location.

## E. Numerical method

System (2) is solved on a Cartesian grid using a high-order finite-difference time-domain (FDTD) algorithm

### 1. Spatial and time derivatives

At the inner points, spatial discretization is performed with explicit fourth-order 11-point centered finite differences optimized to reduce dispersion for wavelengths longer than about five grid spacings.<sup>26</sup> Close to the boundaries, optimized 11-point stencil non-centered finite differences are

TABLE II. Values of the constants used for the atmospheric model.

Ratio of specific heats	$\gamma$	1.4
Specific gas constant	$r$	$287.06 \text{ J kg}^{-1} \text{ K}^{-1}$
Prandtl number	Pr	0.72
Reference temperature	$T_{\text{ref}}$	293.15 K
Sutherland's temperature	$T_s$	117 K
Reference viscosity	$\mu_{\text{ref}}$	$1.8192 \times 10^{-5} \text{ Pa s}$
Gravity constant	$g$	$9.81 \text{ m s}^{-2}$

and

$$q'_i = -\frac{\mu c_p}{\text{Pr}} \frac{\partial T'}{\partial x_i}, \quad (4)$$

where  $\mu$  is the dynamic viscosity, Pr is the fluid's Prandtl number and  $c_p = \gamma r / (\gamma - 1)$  the specific heat at constant pressure. Finally, the dynamic viscosity is calculated as<sup>9</sup>

$$\mu(T) = \mu_{\text{ref}} \left( \frac{T}{T_{\text{ref}}} \right)^{3/2} \frac{T_{\text{ref}} + T_s}{T + T_s}. \quad (5)$$

It is worth emphasizing that, except for the viscous and thermal terms, system (2) is mathematically equivalent to the classical Navier-Stokes equations as long as the mean flow fields are invariant in the  $x_1$  direction.

The numerical values of all the constants are provided in Table II.

## D. Definition of the infrasound source

The source of infrasound is implemented as a time-dependent forcing term  $\Lambda_s$  in the energy equation<sup>17,22</sup>

used.<sup>27</sup> Time integration is carried out by a six-step second-order low-storage Runge-Kutta algorithm.<sup>26</sup>

### 2. Selective and shock-capturing filtering

At the end of each time step, spatial low-pass filtering is performed on the perturbations of conservative variables  $U' = (\rho - \bar{\rho}, \rho u_1 - \bar{\rho} \bar{u}_1, \rho u_2 - \bar{\rho} \bar{u}_2, \rho e_t - \bar{\rho} \bar{e}_t)$  to damp out grid-to-grid oscillations and ensure numerical stability.<sup>26</sup> For this purpose, an explicit sixth-order 11-point stencil filter, designed to remove fluctuations discretized by less than four grid points per wavelength, while leaving larger wavelengths unaffected,<sup>28</sup> is used with a strength  $\sigma^{\text{sf}}$  equal to 0.1.<sup>26</sup> Additionally, a shock-capturing procedure is employed to handle acoustic shocks which are generated during the propagation for sufficiently large source amplitudes. Interested readers can find a detailed description of the methodology in Appendix B.

### 3. Boundary conditions

Near the wall, viscous and thermal effects are expected to be negligible for the considered acoustic wavelengths. Accordingly, only the velocity in the  $x_2$  direction is set to 0, whereas no condition is imposed on the other conservative variables, which are advanced in time by solving the Navier-Stokes equations. Indeed, to implement a no-slip condition, a refinement of the mesh near the ground would be necessary

in order to correctly describe the evolution of the boundary layers. At the left, right, and top boundary, Tam and Dong's<sup>33</sup> radiation condition is applied.

Sponge zones are based on the combination of a Laplacian spatial filtering with grid stretching to dissipate outgoing disturbances and reduce reflections.<sup>34</sup> A specific implementation is required for the top sponge zone to take into account the amplification of waves due to gravity stratification.<sup>22</sup> More specifically, in this zone the gravity profile is progressively reduced from  $g$  to  $-g$ . Once negative gravity has been reached, the ratio of pressure fluctuations to ambient pressure no longer increases but decreases, allowing standard grid stretching techniques and low-order dissipation to operate as in typical sponge zones.

#### 4. Parameters and performance

The entire computational domain contains  $7168 \times 2560 \simeq 20 \times 10^6$  grid points with a grid spacing of  $\Delta = \Delta x_1 = \Delta x_2 = 100$  m. In the present simulations, as a result of the high values of the kinematic viscosity  $\nu = \mu/\rho$  reached in the upper atmosphere, the time step  $\Delta t$  is constrained by the viscous and thermal fluxes rather than by the advection term. To alleviate this constraint, the value of  $\mu$  above the physical domain is progressively reduced down to 0 in the top sponge zone. The Courant-Friedrichs-Lewy and Fourier numbers are defined here, respectively, as  $\text{CFL} = \bar{c}_u \Delta t / \Delta$  and  $\text{Fo} = \bar{\nu}_u \Delta t / \Delta^2$ , where the subscript  $u$  indicates the *upper* boundary of the physical domain, i.e.,  $x_2 = 180$  km. It is found that Fo should be lower than around  $\text{Fo}_{\text{max}} = 0.4$  to avoid numerical instabilities, so that, with  $\Delta = 100$  m, the maximum allowed time step  $\Delta t_{\text{max}} \simeq 0.4 \Delta^2 / \bar{\nu}_u$  is about 0.045 s. For all the computations,  $\Delta t$  is set to 1/30 s, which yields a CFL number of 0.2 and a Fourier number of 0.287. Simulations are carried out until  $t_{\text{max}} = 2800$  s, corresponding to 84 000 time steps.

The numerical algorithm is implemented in the OpenCL language and runs on a AMD Radeon R9 200 Series GPU with a memory allocation limit of 4 GB. A comparative study of the computational time required on a variety of CPUs and GPUs was carried out by Marsden *et al.*<sup>22</sup> Performance on GPUs was found to be considerably higher than on CPUs. For the present computations using the OpenCL code, one time step takes about one second, which leads to a total time duration of about 24 h per simulation.

#### F. Numerical dissipation versus physical dissipation

When system (2) is solved with the algorithm described in Sec. II E, four dissipation mechanisms affect the numerical solution: the physical diffusion due to the molecular viscosity, and numerical dissipation due to the selective filter, the shock-capturing procedure and the time advancement scheme. Spatial derivatives at the inner points of the computational domain are based on centered schemes and do not induce dissipation.<sup>26</sup> In order to compare the different contributions, the transfer functions of all these mechanisms<sup>24,35</sup> are evaluated as a function of the normalized wavenumber  $k\Delta$ . The dissipation transfer function  $\mathcal{F}_\nu$  associated with the molecular viscosity is given by  $\bar{\nu} k^2$ , yielding  $\mathcal{F}_\nu(k\Delta) = \bar{\nu} (k\Delta)^2 / \Delta^2$ .

Regarding the selective filtering procedure, which is applied to the flow variables at every time step  $\Delta t$ , the transfer function can be written as<sup>26</sup>  $\mathcal{F}^{\text{sf}}(k\Delta) = (\sigma^{\text{sf}} / \Delta t) \mathcal{D}^{\text{sf}}(k\Delta)$ , where  $\mathcal{D}^{\text{sf}}$  is the Fourier transform of the operator  $D^{\text{sf}}$ . The same reasoning can be applied to the shock-capturing procedure. Its transfer function is  $\mathcal{F}^{\text{sc}}(k\Delta) = (\sigma^{\text{sc}} / \Delta t) \mathcal{D}^{\text{sc}}(k\Delta)$ , where  $\mathcal{D}^{\text{sc}}$  is the Fourier transform of the second-order filter used in the procedure<sup>28</sup> and  $\sigma_{\text{max}}^{\text{sc}}$  its maximum strength, which is here set equal to 0.25. Finally, the dissipation transfer function linked to the time integration  $\mathcal{F}^{\text{ts}}$  is given by  $\mathcal{F}^{\text{ts}}(k\Delta) = [1 - |G(\omega\Delta t)|] / \Delta t$ , where  $|G(\omega\Delta t)|$  is the amplification factor per time step of the Runge-Kutta algorithm.<sup>27</sup> The normalized pulsation  $\omega\Delta t$  is computed as  $\omega\Delta t = \bar{c}_u(k^*\Delta)\Delta t / \Delta$ , where  $k^*$  denotes the approximated wavenumber provided by the finite difference scheme.

The transfer functions are plotted in Fig. 3. In particular, the dissipation transfer function  $\mathcal{F}_\nu$  is shown for three different altitudes of 50, 80, and 100 km. For the spacing  $\Delta$  used here, the dissipation due to time integration is negligible compared to that of the selective filtering. At altitudes where absorption phenomena become important, namely, above 100 km in the present cases, physical dissipation is found to be stronger than the filtering dissipation, at least for the well resolved wavenumbers below  $k\Delta = \pi/2$ . Finally, the shock-capturing procedure is highly dissipative, but, according to the sensor strength in Eq. (B4), it is applied only near the shocks and not in the smooth regions of the solution. The molecular absorption phenomena are thus correctly taken into account in the upper atmosphere by the present numerical algorithm.

### III. RESULTS

One of the most spectacular features of infrasound propagation in the atmosphere is the observation at ground level of signals, also called *phases*, that have reached very high altitudes during their propagation. These various arrivals are generated by downward refraction stemming in large part from the atmospheric mean speed of sound profile  $\bar{c}(x_2)$ ,

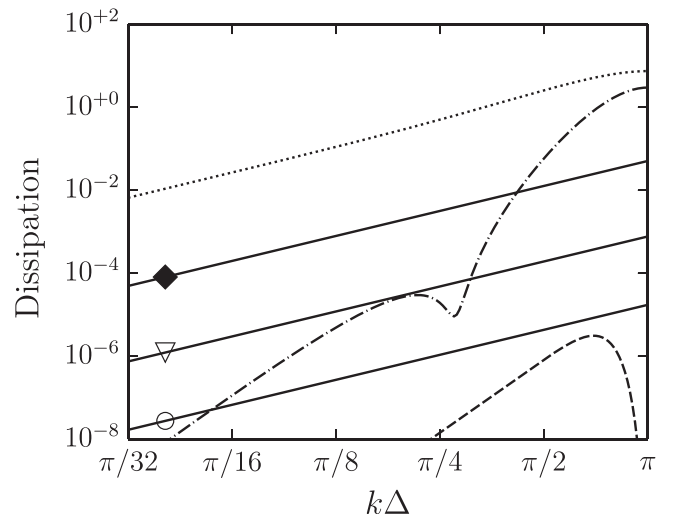


FIG. 3. Dissipation transfer functions.  $\mathcal{F}_\nu$  at 50 km ( $\circ$ ), 80 km ( $\nabla$ ) and 100 km ( $\blacklozenge$ ),  $\mathcal{F}^{\text{sf}}$  (dash dotted line),  $\mathcal{F}^{\text{sc}}$  (dotted line),  $\mathcal{F}^{\text{ts}}$  (dashed line).

TABLE III. Simulation parameters.

Case	Wind profile	Source parameters			Energy flux	Max. overpressure
		$\mathcal{A}_s$ ( $\text{J m}^{-3} \text{s}^{-1}$ )	$f_s$ (Hz)	$b_s$ (m)	$I_a$ ( $\text{J m}^{-1}$ )	$\max_t(p')$ (Pa)
L	no wind	$1.0 \times 10^{-1}$	0.1	600	$1.066 \times 10^{-2}$	$2.62 \times 10^{-2}$
LW	$\bar{u}_1(x_2)$	$1.0 \times 10^{-1}$	0.1	600	$1.066 \times 10^{-2}$	$2.62 \times 10^{-2}$
NL	no wind	$2.5 \times 10^{+2}$	0.1	600	$6.662 \times 10^{+4}$	$6.48 \times 10^{+1}$
NLW	$\bar{u}_1(x_2)$	$2.5 \times 10^{+3}$	0.1	600	$6.673 \times 10^{+6}$	$6.59 \times 10^{+2}$

which increases with altitude both in the stratosphere and the thermosphere, as shown in Fig. 2(a). The infrasonic waves are continuously refracted downward as they cross the atmospheric layers and propagate along periodic arched paths which curve toward the Earth’s surface. Because of successive reflections from the land surface, such rays form acoustic light and shadow zones even at long distances from the source.<sup>5</sup> A first case, labeled L (*Linear*), is defined to underline this waveguide effect. A weak source amplitude  $\mathcal{A}_s$  is chosen, in order for nonlinear terms to be negligible,<sup>22</sup> and the atmosphere is specified to be at rest.

Alongside the downward refraction due to the profile of sound speed, the presence of strong wind also induces possible refraction phenomena. Depending on its profile, temperature-related ducting can be amplified or attenuated, and, furthermore, additional acoustic signals can be recorded at ground level.<sup>29</sup> To highlight these aspects, the aforementioned horizontal wind profile is included in a second case denoted LW (*Linear with Wind*).

Real-world problems usually involve strong source amplitudes, which result in significant modifications to the waveforms recorded at ground levels.<sup>30</sup> To evaluate the importance of non-linearities, the previous configurations are reexamined with larger and more realistic source amplitudes. Two cases, labeled NL (*Nonlinear*) and NLW (*Nonlinear with Wind*), are thus designed. The main numerical parameters of the four selected configurations are summarized in Table III.

As highlighted by Bergmann,<sup>36</sup> the amplitude of pressure fluctuations is proportional to the square root of the mean density. The following normalized pressure fluctuation is therefore defined

$$\Phi(x_1, x_2, t) = \frac{p(x_1, x_2, t) - \bar{p}(x_2)}{\mathcal{A}_s \sqrt{\bar{\rho}(x_2)}}. \quad (7a)$$

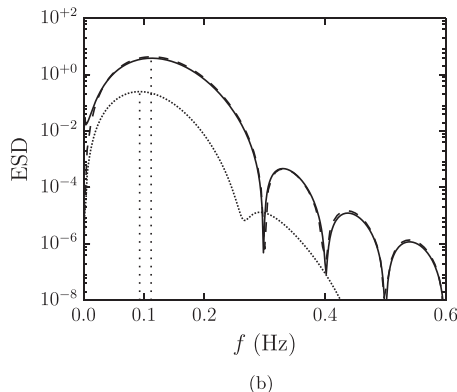
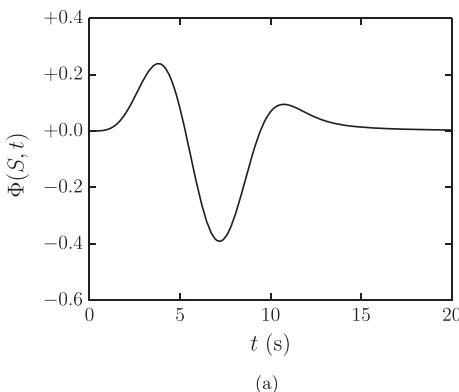


FIG. 4. NLW case. (a) Normalized pressure  $\Phi$  [Eq. (7a)] recorded at the source location  $S$ . (b) One-sided energy spectral density ESD [Eq. (7c)] of the normalized pressure  $\Phi$  at points  $S$  (solid line) and  $B_1$  (dotted line); exact solution of the Helmholtz equation for a homogeneous medium at  $S$  (dashed line).

The source amplitude  $\mathcal{A}_s$  is introduced to allow comparisons between the different cases. The maximum overpressure at ground level

$$\Phi_g(x_1) = \max_t \Phi(x_1, x_2 = 0 \text{ km}, t) \quad (7b)$$

is studied as well. The pressure signature is analyzed in the frequency domain, through its one-sided energy spectral density

$$\text{ESD}(x_1, x_2, f) = 2 \left| \int_{-\infty}^{+\infty} \Phi(x_1, x_2, t) e^{-2\pi i f t} dt \right|^2, \quad f \in \mathbb{R}^+. \quad (7c)$$

In particular, the ESD computed on the  $x_1$  and  $x_2$  axes, that is  $\text{ESD}_1 = \text{ESD}(x_1, 0 \text{ km}, f)$  and  $\text{ESD}_2 = \text{ESD}(0 \text{ km}, x_2, f)$ , are investigated. To characterize the infrasound source, two parameters are examined, the peak overpressure at the source location  $P_s = \max_t(p(S, t) - \bar{p}_g)$  and the energy flux  $I_a$ , calculated according to

$$I_a = \int_0^{t_\infty} \left( \int_\Sigma (p - \bar{p})(\mathbf{u} - \bar{\mathbf{u}}) \cdot d\mathbf{l}_\Sigma \right) dt, \quad (7d)$$

where the surface  $\Sigma$  is chosen as the boundary of the domain  $[-5, +5] \times [0, 10] \text{ km}^2$  (see Fig. 1). The integral in Eq. (7d) is to be calculated up to a time  $t_\infty$  sufficiently large for the wavefront emitted by the source to cross the integration line.

## A. Overview of results

### 1. Characterization of the infrasonic source

The normalized pressure  $\Phi$  recorded at the source location  $S$  for the NLW case is plotted in Fig. 4(a), along with the corresponding one-sided energy spectral density ESD [Fig. 4(b)]. The peak overpressure  $P_s$  detected at the point  $S$  is of about 598.4 Pa and the frequency corresponding to the maximum ESD is around 0.11 Hz. The waveform at  $S$  is found to be nearly independent from both the source amplitude  $\mathcal{A}_s$  and the presence of wind, at least for values of  $\mathcal{A}_s$  up to  $10^4 \text{ J m}^{-3} \text{ s}^{-1}$ . This result is also confirmed by the good agreement between the present numerical solution and the analytical ESD obtained by solving the classical Helmholtz equation for a homogeneous medium [see Fig. 4(b)]. For the range of amplitudes considered here, the peak overpressure

$P_s$  scales approximately as  $\mathcal{A}_s/4$ . The one-sided energy spectral density ESD of the signal recorded at point  $B_1 = (0 \text{ km}, 5 \text{ km})$  is also reported in Fig. 4(b). A slight shift toward a lower value of the frequency corresponding to the maximum ESD is observed as a result of the non-compactness of the source, whose Helmholtz number  $\text{He} = k_s b_s = 2\pi f_s b_s / \bar{c}(S)$  is around 1.1. The Gaussian source distribution acts as a low-pass filter applied to the source term  $\Lambda_s$ . The intensity  $I_a$  [Eq. (7d)] is also found to be almost independent from the presence or not of the wind, and it scales as  $I_a \sim \mathcal{A}_s^2$ . Values of  $P_s$  and  $I_a$  for the four configurations are reported in Table III.

## 2. Linear case

Some snapshots of the normalized pressure  $\Phi$  obtained with  $\mathcal{A}_s = 10^{-1} \text{ J m}^{-3} \text{ s}^{-1}$  are shown in Fig. 5 for different time instants. Acoustic rays are also superimposed. Owing to the vertically stratified speed of sound, acoustic waves are refracted while propagating through the atmosphere. A waveguide is generated between the Earth's surface and about 110 km altitude, where the speed of sound becomes greater than its value at ground level.<sup>5</sup> Consequently, the wavefront emitted by the infrasonic source rapidly loses its cylindrical shape visible in Fig. 5(a). Various arrivals are observed at ground level, depending on the distance from the source. Up to about  $x_1 = 140 \text{ km}$  range, only the direct phase, noted  $I_w$ , is recorded. Its amplitude decays exponentially with the distance along the  $x_1$ -axis.<sup>10,37</sup> This diminution is not attributed to physical dissipation, but to a more complex redistribution of energy in the waveguide. Indeed, a stratospheric phase is rapidly generated. It is clearly visible in Fig. 5(b) at about 40 km altitude, where the lower part of the wavefront begins to split into two different arrivals. The new phase is not predicted by ray theory, since associated with low-frequency or diffraction phenomena. It is refracted toward the ground around the altitude of the local maximum of the speed of sound profile, whose value is relatively close to the celerity at ground level. It is labeled  $I_{s1}$ . At  $t = 700 \text{ s}$ , a strong cusp caustic appears around 113 km altitude [Fig. 5(c)]. The acoustic rays which have reached the thermosphere now turn toward the Earth's surface. The refracted wave consists of two wavefronts generated by the lower and higher thermospheric rays. As a result of the diffraction at the caustic, the amplitude of the associated thermospheric phases, noted, respectively,  $I_{ta1}$  and  $I_{tb1}$ , becomes appreciable at about  $x_1 = 200 \text{ km}$  [Fig. 5(d)], whereas the arrival range predicted by ray theory is around 290 km. At larger distances from the source, in spite of a longer path length, the higher thermospheric wave  $I_{tb1}$  arrives before the lower phase  $I_{ta1}$  thanks to the greater propagation speed in the upper atmosphere. For simulation times larger than about 1200 s, the fluctuating pressure field becomes more and more complex and a multitude of arrivals reaches the Earth's surface. Along with the two thermospheric phases, arch-like wavefronts are generated in the waveguide [Fig. 5(e)]. Besides, the thermospheric rays reflected by the ground are again refracted back toward the Earth's surface. The subsequent thermospheric phases,

labeled  $I_{ta2}$  and  $I_{tb2}$ , hit ground more than 500 km away from the source [Fig. 5(f)].

In order to gain more insight into the generation of the arch-like wavefronts, which cannot be captured by ray theory, a zoom of  $\Phi$  at three different times is reported in Fig. 6. At 1000 s, the wavefront  $W_{s1}^r$ , produced by the reflection of the first stratospheric phase  $I_{s1}$ , propagates upward [Fig. 6(a)]. At about 49 km altitude [Fig. 6(b)],  $W_{s1}^r$  is partially reflected down toward the ground ( $W_{s2}^i$ ) and partially transmitted into the mesosphere ( $W_{s1}^t$ ). This waveguide effect is induced by the variations of the mean speed of sound: it has a local maximum at  $x_2 = 49 \text{ km}$ , which is close to its value at ground level. When the wavefront  $W_{s2}^i$  reaches the ground, a new stratospheric phase, labeled  $I_{s2}$ , is recorded.  $W_{s2}^i$  is in turn reflected by the Earth's surface, so that the process of generation of a new arch structure starts again [Fig. 6(c)]. More generally, partial reflections and transmissions around  $x_2 = 49 \text{ km}$  can be observed whenever a wavefront propagates downward or upward in the stratosphere. An example is given in Fig. 6(c), where a new arch is generated by the wavefront  $W_{ta1}^i$  associated with the first thermospheric phase.

The normalized pressure  $\Phi$  recorded at the ground station  $S_1 = (300 \text{ km}, 0 \text{ km})$  is shown in Fig. 7(a). Two different arrivals can be distinguished: the first stratospheric phase,  $I_{s1}$ , between 980 and 1040 s, and a combination of the first lower and upper thermospheric phases,  $I_{ta1}$  and, between 1220 and 1280 s. This result is in good agreement with the geometrical acoustic theory, which yields an arrival time of about  $t = 1240 \text{ s}$  for  $I_{ta1}$ . Furthermore, the thermospheric waveform coincides with the Hilbert transform of the signal recorded at the source location, as expected for rays passing through a caustic.<sup>10</sup>

The normalized pressure  $\Phi$  recorded at the ground station  $S_2 = (600 \text{ km}, 0 \text{ km})$  is shown in Fig. 7(b). Several arrivals can be observed: the diffracted stratospheric arrivals and the thermospheric ones. As at  $S_1$ , the maximum overpressure is due to the lower thermospheric phases. Furthermore, a phase shift can be again noticed on the signal  $I_{ta2}$ .

The normalized pressure  $\Phi$  recorded at ground level is illustrated in Fig. 8(a) as a function of the distance from the source  $x_1$  and of the reduced time  $t_r = t - x_1 / \bar{c}(0 \text{ km})$ , to better visualize the various phases and their arrival times. Additionally, the normalized maximum overpressure  $\Phi_g$  is shown in Fig. 8(b), along with the contributions of the different arrivals. The amplitude of the direct phase  $I_w$  is found to decay faster than the classical two-dimensional cylindrical spreading behavior,  $\Phi_g \sim x_1^{-1/2}$ . This reduction is attributed to the negative gradient of the speed of sound near the ground, which deviates the acoustic rays toward higher altitudes.<sup>10,37</sup> At about  $x_1 = 100 \text{ km}$ , the maximum overpressure of  $I_w$  is found to be 1% of the value at the origin of the domain. The direct phase  $I_w$  is recorded almost without delay since it propagates at a speed close to the celerity at ground level. The first diffracted arrival  $I_{s1}$  is recorded with an appreciable level at distances from the source greater than 140 km, and at a reduced time between 110 and 160 s. This means that the overpressure induced by this phase is delayed by about 110 s with respect to a hypothetical direct wave.

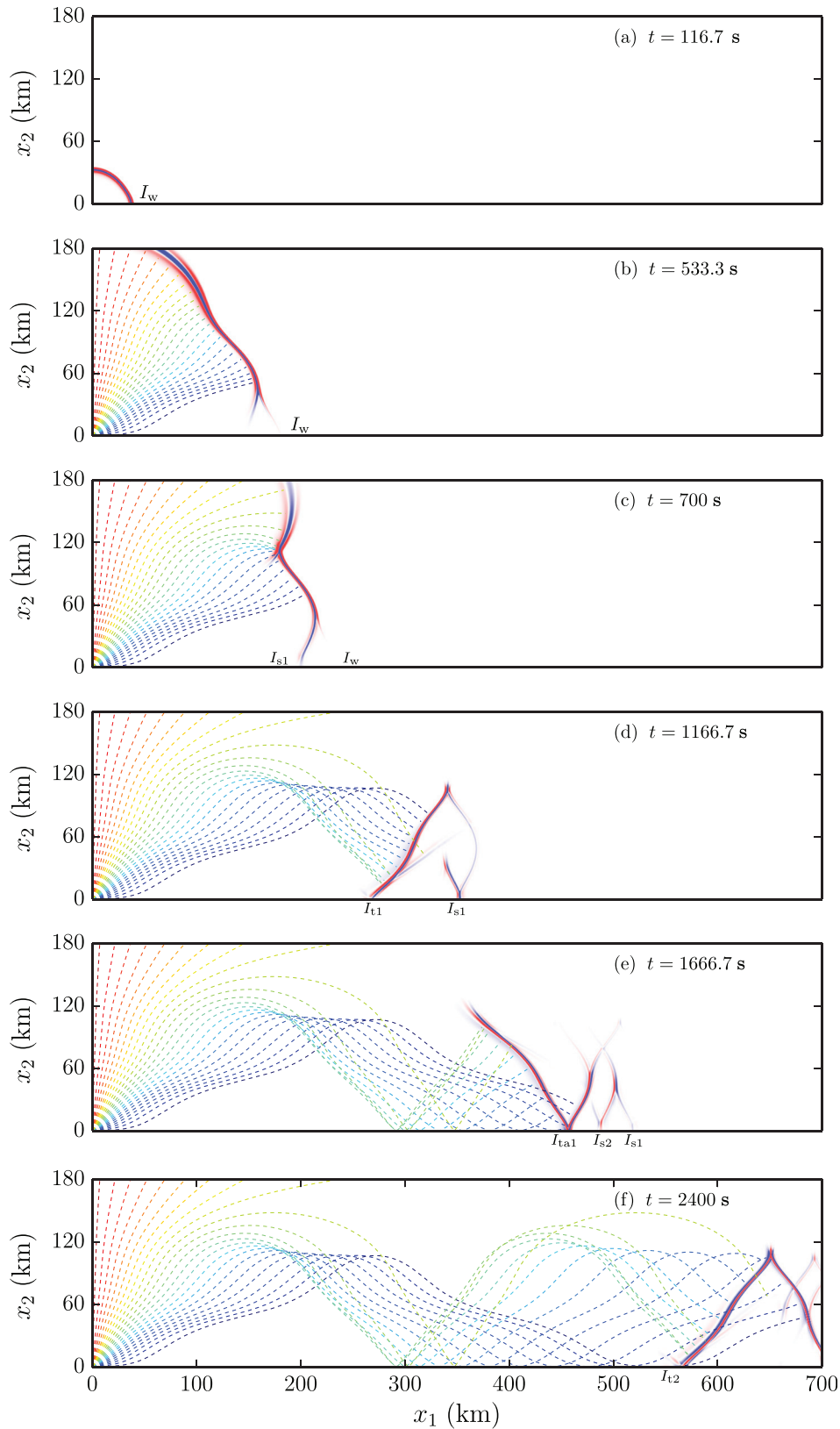


FIG. 5. L case. Snapshots of the normalized pressure  $\Phi$  at different time instants.

The first thermospheric phases are detected with non negligible amplitudes for  $x_1 > 200$  km at a reduced time which diminishes with increasing distance  $x_1$ . The higher arrival  $I_{tb1}$ , which travels faster than the lower phase  $I_{ta1}$ , is even recorded at  $x_1 = 600$  km with no delay. Between  $x_1 = 400$  km and  $x_1 = 500$  km, a second diffracted arrival  $I_{s2}$  is generated. It is detected with a delay of about 250 s. Finally,

the second thermospheric arrivals,  $I_{ta2}$  and  $I_{tb2}$ , become detectable for distances from the source greater than 500 km and with a delay of around 750 s. Beyond the first geometrical shadow zone, the function  $\Phi_g$  exhibits a peak at about  $x_1 = 300$  km, as a consequence of the first lower thermospheric arrival  $I_{ta1}$ ; the phase  $I_{ta1}$  is responsible for the maximum overpressure visible between  $x_1 = 300$  km and

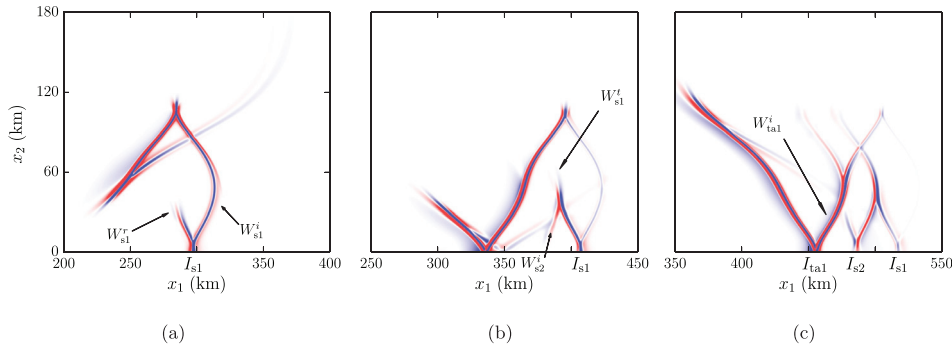


FIG. 6. L case. Zoom of the snapshots of the normalized pressure  $\Phi$  at (a) 1000 s, (b) 1333.3 s, and (c) 1666.7 s.

$x_1 = 600$  km; over this range,  $\Phi_g$  is about 5% to 10% of the overpressure measured at the source location  $S$ .

The spectrogram  $ESD_1$  of the signals detected at ground level is reported in Fig. 8(c), where color indicates the ESD level as a function of frequency  $f$  for each recording location  $x_1$ . Most of the energy is found around the source frequency  $f_s = 0.1$  Hz, even at distances larger than 200 km from the source, where the maximum overpressure is due in large part to the thermospheric phases. This is a consequence of the small source amplitude  $\mathcal{A}_s$ : nonlinear effects are not appreciable. By integrating the ESD function over  $x_1$  and  $f$ , it is found that about 99.3% of the energy is associated with frequencies in the interval  $[0 \text{ Hz}, 0.2 \text{ Hz}]$ .

The ESD computed along the  $x_2$  axis is plotted in Fig. 9(a) as a function of frequency  $f$  and distance from the source  $x_2$ . As a result of the small source amplitude, the signal  $\Phi$  undergoes negligible distortion during its vertical propagation up to about 120 km. Below 120 km, and outside the source region, the frequency  $f_p(x_2)$  of the maximum  $ESD_2$  for a given altitude  $x_2$  remains constant with a value of  $f_p \simeq 0.093$  Hz. Furthermore, until 120 km, the amplitude of the pressure fluctuations decreases, owing essentially to the cylindrical spreading.

For higher altitudes, thermoviscous dissipation becomes increasingly important due to the exponential diminution of the mean density, as also demonstrated by the departure of the Navier-Stokes result from that of the Euler model. The

signal amplitude drops, and a shift toward lower frequencies is observed, since absorption phenomena depend not only on the value of the kinematic viscosity  $\bar{\nu}$  but also on the square of the frequency.<sup>9,10</sup> The frequency  $f_p$  is about 0.042 Hz at  $x_2 = 180$  km.

### 3. Linear with Wind case

The presence of a wind profile in the atmosphere generally has a strong impact on the acoustic field recorded at ground level. The arrival time of the different phases as well as their amplitude and waveform are affected.<sup>29,38</sup> The generation of new arrivals can be also observed. As an illustration, a snapshot of  $\Phi$  at  $t = 666.7$  s is shown in Fig. 10. Acoustic rays are also superimposed. The initially isotropic wavefront is deformed by the stratification of the mean atmosphere.

Furthermore, a caustic appears at an altitude of about 111 km. The influence of the wind profile on the acoustic field is clearly visible at stratospheric and mesospheric altitudes, where multiple reflections toward the Earth's surface are generated. In particular, a second caustic is formed at a height of about 45 km, where the effective speed of sound  $\bar{c}_{\text{eff}} = \bar{c} + \bar{u}_1$  exceeds its ground level value<sup>5,10</sup> [see Fig. 2(a)]. The amplitude of the subsequent stratospheric arrival  $I_{s1}$  becomes noticeable at about  $x_1 = 150$  km. This value should be compared to the arrival range predicted by the geometrical acoustic theory, of around 270 km. Moreover,

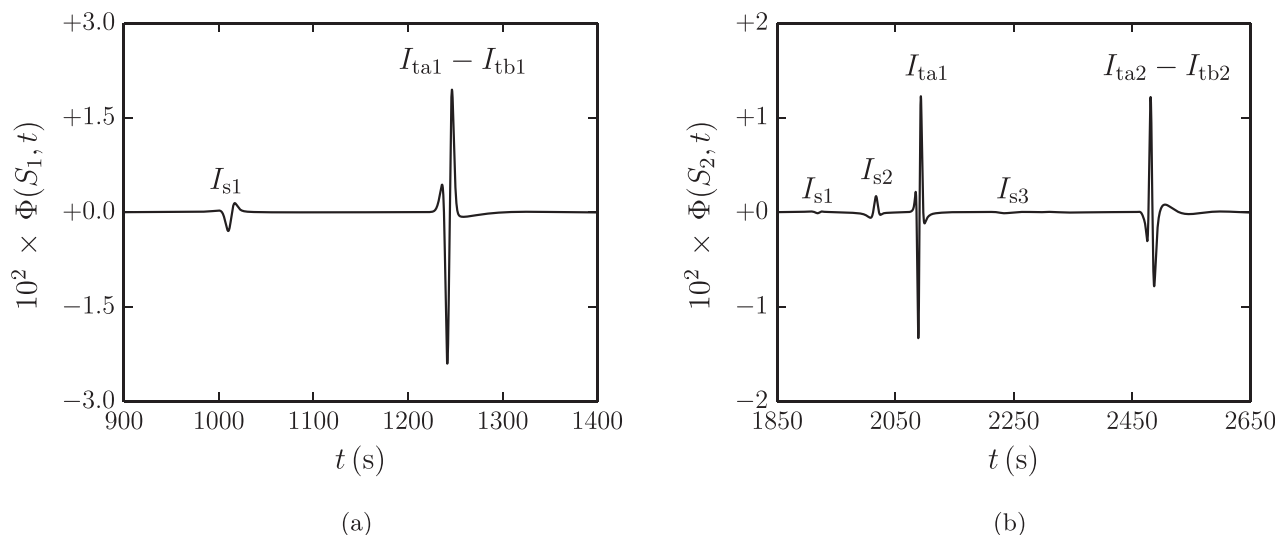


FIG. 7. L case. Normalized pressure  $\Phi$  recorded at stations (a)  $S_1$  and (b)  $S_2$ .

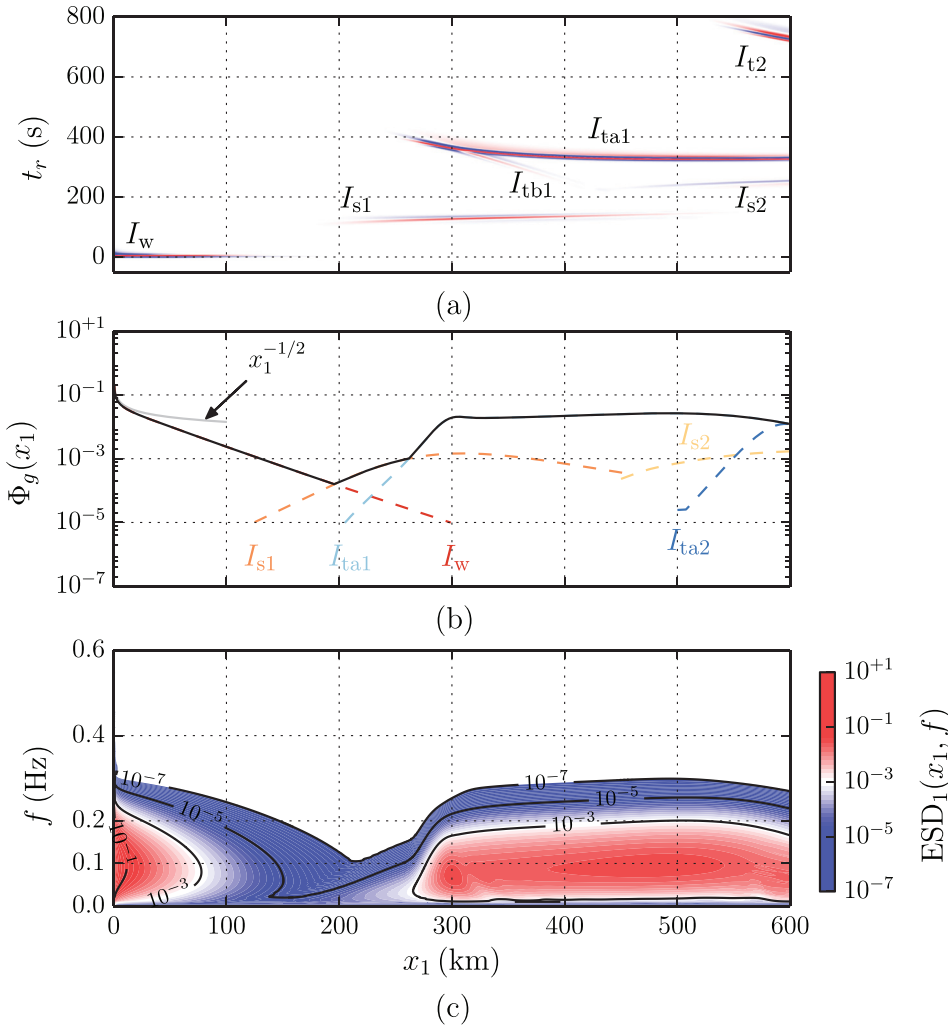


FIG. 8. L case. Ground recordings: (a) normalized pressure  $\Phi$  as a function of range  $x_1$  and of reduced time  $t_r$ ; (b) normalized maximum overpressure  $\Phi_g$  at ground level; (c) spectrogram  $ESD_1$  of  $\Phi$  as a function of  $x_1$  and frequency  $f$ .

an additional reflection is observed around  $x_2 = 70$  km, near a local maximum of the effective speed of sound. This diffracted phase is labeled  $I_{m1}$ .

The pressure signal  $\Phi$  recorded at the ground station  $S_3 = (270 \text{ km}, 0 \text{ km})$  is shown in Fig. 11(a). The signal obtained without wind is also reported in light gray for comparison. The thermospheric signature remains almost untouched by the horizontal wind. The amplitude is however doubled, and the arrival time, reduced. The time lag between the maximum overpressures is of about 35 s, corresponding to a difference between the apparent propagation speeds of  $7.06 \text{ m s}^{-1}$ . The mean atmospheric profile considerably reinforces the stratospheric ducting. The stratospheric arrival  $I_{s1}$

has an amplitude 20 times higher than that of the diffracted phase  $I_{s1}$  recorded in the absence of wind. The time lag between the maximum stratospheric overpressures is of 15 s. The signature detected in the presence of wind is also modified. Since it passes through the stratospheric caustic, it exhibits a shape close to the Hilbert transform of the signal recorded at the source location. The additional mesospheric phase has a very low amplitude, about two orders of magnitude smaller than the stratospheric signal.

The maximum overpressure  $\Phi_g$  at ground level is plotted in Fig. 11(b) as a function of  $x_1$ . The contributions of the different phases are reported in dashed line; the result obtained without wind is also plotted in gray.

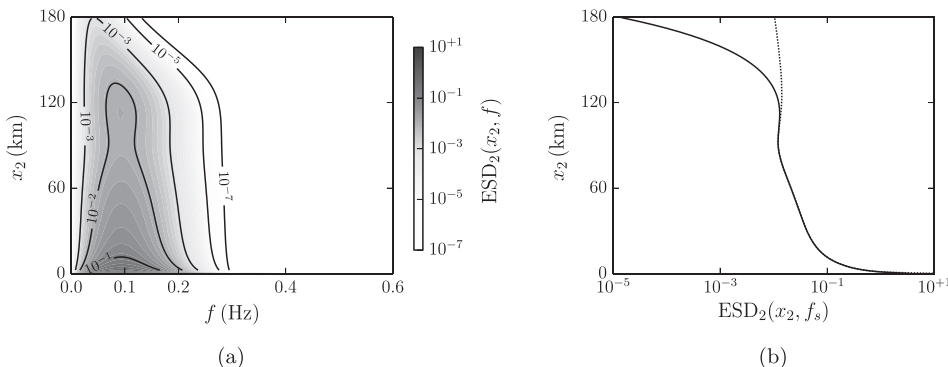


FIG. 9. L case. (a) ESD of the whole signal recorded along the  $x_2$  axis and above the source; (b) ESD profile for  $f=f_s$  obtained by the Navier-Stokes model (black solid line) and without viscous and thermal terms (dotted line).

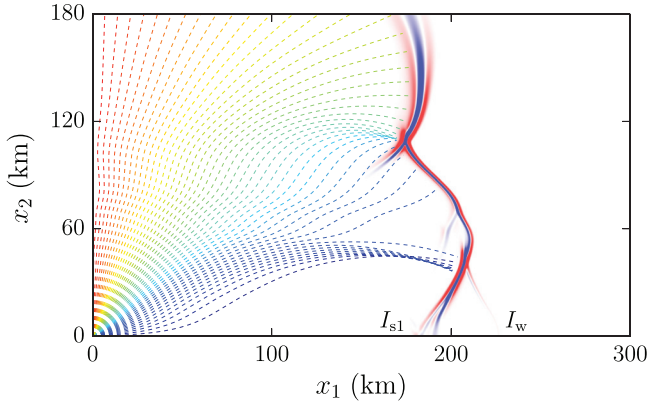


FIG. 10. LW case. Snapshot of the normalized pressure  $\Phi$  at  $t = 666.7$  s.

The decay rate of the amplitude of the direct phase is reduced in the presence of wind. A moving medium with velocity  $\bar{u}_1$  and speed of sound  $\bar{c}$  can be considered to a first approximation as a medium at rest with an effective speed of sound  $\bar{c}_e = \bar{c} + \bar{u}_1$  (Ref. 13) [see Fig. 2(a)]. Considering that the wind profile is globally positive near the ground, the decay rate diminishes as the effective celerity gradient is decreased by the horizontal flow. Finally, beyond the shadow zone and except for distances from the source between roughly 350 and 520 km, the generally larger amplitude of the stratospheric arrivals induced by the horizontal wind produces an increase in the peak overpressure measured at ground level.

#### 4. Nonlinear case

The amplitude of the infrasonic source is found to have a negligible influence on the geometrical structure of the acoustic field: the number and features of arrivals remain the same, at least for the cases under study. However, the signature recorded at a given distance  $r$  is highly affected by nonlinear effects. For large source amplitudes  $\mathcal{A}_s$ , the initially smooth wavefront is distorted during propagation and, at a characteristic distance  $r_{\text{shock}}$ , which decreases with  $\mathcal{A}_s$ ,

shock waves are formed. To highlight this aspect, the normalized pressure  $\Phi$  recorded at three different altitudes along the  $x_2$  axis,  $B_2 = (0 \text{ km}, 80 \text{ km})$ ,  $B_3 = (0 \text{ km}, 120 \text{ km})$  and  $B_4 = (0 \text{ km}, 170 \text{ km})$ , is plotted in Fig. 12.

At the point  $B_2$ ,  $\Phi$  is still a smooth function, but its waveform has undergone appreciable modifications from the source [see Fig. 12(a) and 4(a)]. Moreover, its amplitude has diminished by a factor 20 as a consequence of the two-dimensional cylindrical spreading. The waveform steepens with increasing time and distance and evolves into an N-shaped wave [Fig. 12(b)]. Once the N-wave is formed, it lengthens while propagating toward the upper atmosphere [Fig. 12(c)]. Its duration is about 25 s at  $B_3$  and 50 s at  $B_4$ . The importance of the viscous and thermal terms is again emphasized in Fig. 12(c), where the signal resulting from the Euler equations is also reported in gray. The maximum overpressure is almost halved by the thermoviscous absorption phenomenon. The central part of the wave and the frequency  $f_p$  of the maximum ESD<sub>2</sub> remains however untouched.

The ESD computed along the  $x_2$  axis is displayed in Fig. 13(a). The shock formation coincides with a rapid widening of the spectrum. For distances from the source smaller than about 40 km, most of the energy is around the source frequency, whereas above 40 km, the energy of higher harmonics becomes significant. The behavior of the ESD as a function of altitude is shown in Fig. 13(b) for three different spectral component frequencies,  $f = nf_s$ , with  $n = 1, 2, 3$ . As the shock formation implies a transfer of energy toward shorter waves, the energy associated with the fundamental frequency drops with height, whereas the ESD of the harmonics rapidly increases and reaches a maximum value around  $x_2 = 95 \text{ km}$ . For higher altitudes, the lengthening of the N-wave causes a shift of the frequency  $f_p$  toward lower values, and thermoviscous absorption erases higher harmonics. Therefore, a shock formation distance  $x_2^{\text{shock}}$  can be defined here as the distance  $x_2$  from the source at which the ESD of the first harmonic reaches its maximum value,  $x_2^{\text{shock}} \simeq 94.8 \text{ km}$  in the present case.

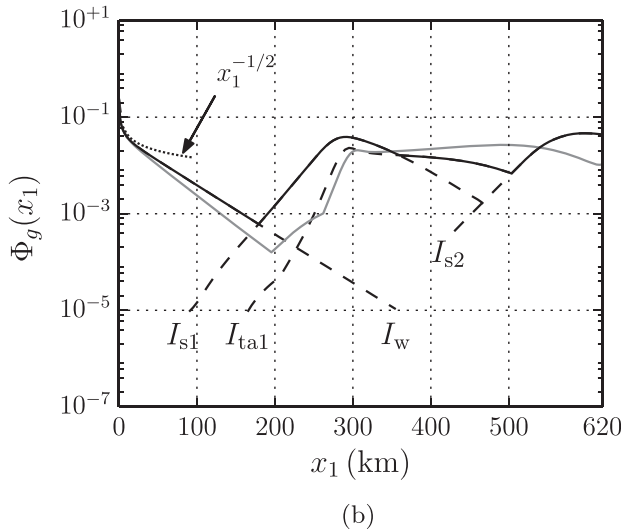
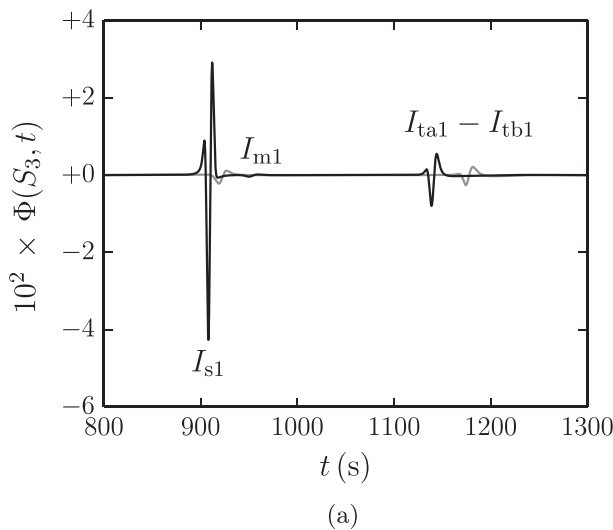


FIG. 11. LW case. (a) Pressure  $\Phi$  recorded at the station  $S_3$ . (b) Maximum overpressure  $\Phi_g$  obtained with (black solid line) and without (gray solid line) wind: contributions of the different phases (dashed line) in the presence of the wind.

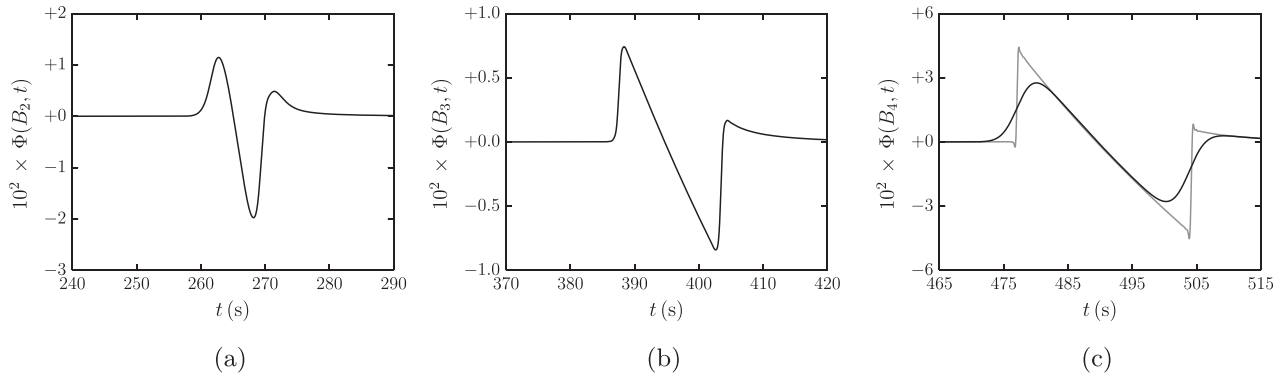


FIG. 12. NL case. Normalized pressure  $\Phi$  recorded at altitudes (a)  $B_2$ , (b)  $B_3$ , and (c)  $B_4$ ; in gray, result obtained without viscous and thermal terms.

It is interesting to note that the diminution of the atmospheric density contributes highly not only to the increase in thermoviscous absorption but also to the development of nonlinear effects. Waveform distortion primarily depends on the term  $\bar{\rho}^{-1/2}$  which varies strongly between the ground and the thermosphere.<sup>39</sup>

The pressure  $\Phi$  recorded at the ground station  $S_1$  is illustrated in Fig. 14. The signal obtained in the L case is also reported in light gray for comparison. The stratospheric arrival  $I_{s1}$  is found to be untouched by nonlinear effects [Fig. 14(a)]: these effects become appreciable beyond the stratospheric waveguide limit, where this phase is refracted back toward the Earth's surface. Conversely, nonlinear distortion has a strong impact on the thermospheric phases  $I_{ta1}$  and  $I_{tb1}$ . The U-shape wave visible in Fig. 14(b) is generated by the N-wave of the lower signal  $I_{ta1}$  which passes through the thermospheric cusp caustic.<sup>6,10,11</sup> Furthermore, as a result of the lengthening of the signal, the peak overpressure is brought forward by about 15 s compared to the arrival time for the lowest source amplitude. The peak overpressure itself is reduced in relative terms by the nonlinear effects.

### 5. Nonlinear with Wind case

The aim of the last study is to investigate the combined effects of non-linearity and wind gradient on the acoustic

field produced by an infrasound source. As in the LW-case, the presence of a wind profile generates a second caustic at about 50 km altitude and tends to magnify the peak overpressure associated with the subsequent stratospheric arrival. Unlike in the NL-case, the source amplitude is now strong enough for non-linear modifications to be significant also on the stratospheric arrival. This aspect is highlighted in Fig. 15(a), which displays the pressure  $\Phi$  recorded at the ground station  $S_3$  corresponding to this phase. Results obtained in the NL and LW cases are also reported for comparison. The stratospheric signal detected in the NLW case is clearly distorted by nonlinear effects. It exhibits a U-shaped waveform, which suggests that an N-wave is generated as rays climb toward the stratosphere before reaching the stratospheric caustic. Following the criterion described in the previous paragraph, shock formation occurs at  $x_2 = 63$  km altitude.

As in the NL case, once the N-wave is created, it lengthens while propagating in the vertical direction. This lengthening corresponds to a shift toward lower frequencies. At  $x_2 = 63$  km,  $f_p$  is about 0.08 Hz, whereas, above  $x_2 = 140$  km,  $f_p$  is around 0.01 Hz. Furthermore, it is found that the frequency  $f_p$  varies as  $\sim 1/(3\tau^+)$ , where  $\tau^+$  represents the duration of the positive phase of the N-wave.<sup>6,40</sup> For the present source amplitude, thermoviscous effects are found to play a minor role on the shape of the signal. When the wavefront arrives in

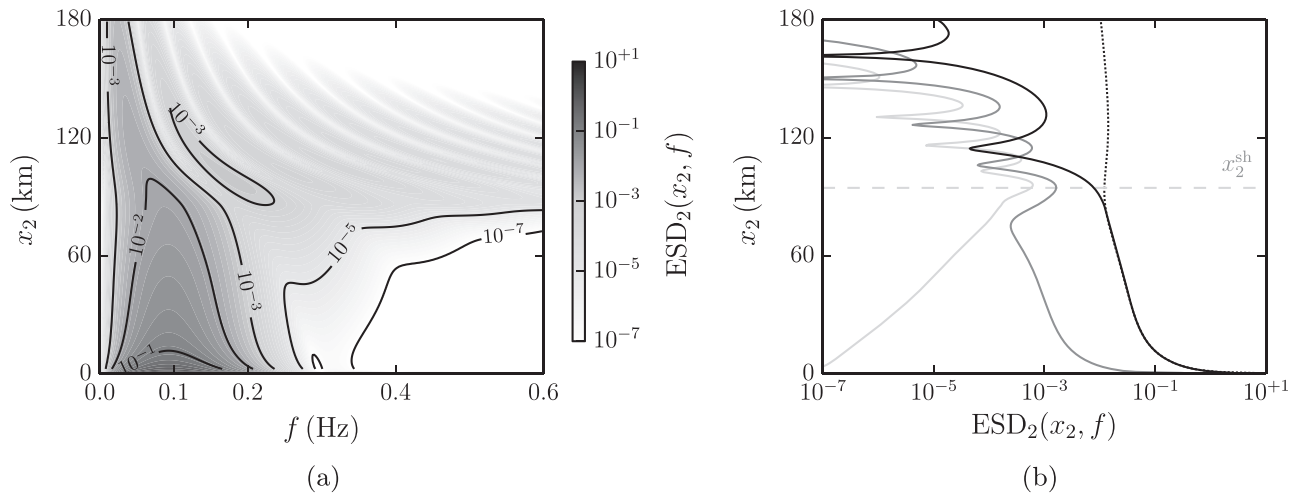


FIG. 13. NL case. (a) ESD of the whole signal recorded along the  $x_2$  axis and above the source; (b) ESD profiles for  $f=f_s$  (black solid line),  $f=2f_s$  (slate gray solid line) and  $f=3f_s$  (light gray solid line); in dotted line, result obtained in the Linear case without viscous and thermal terms.

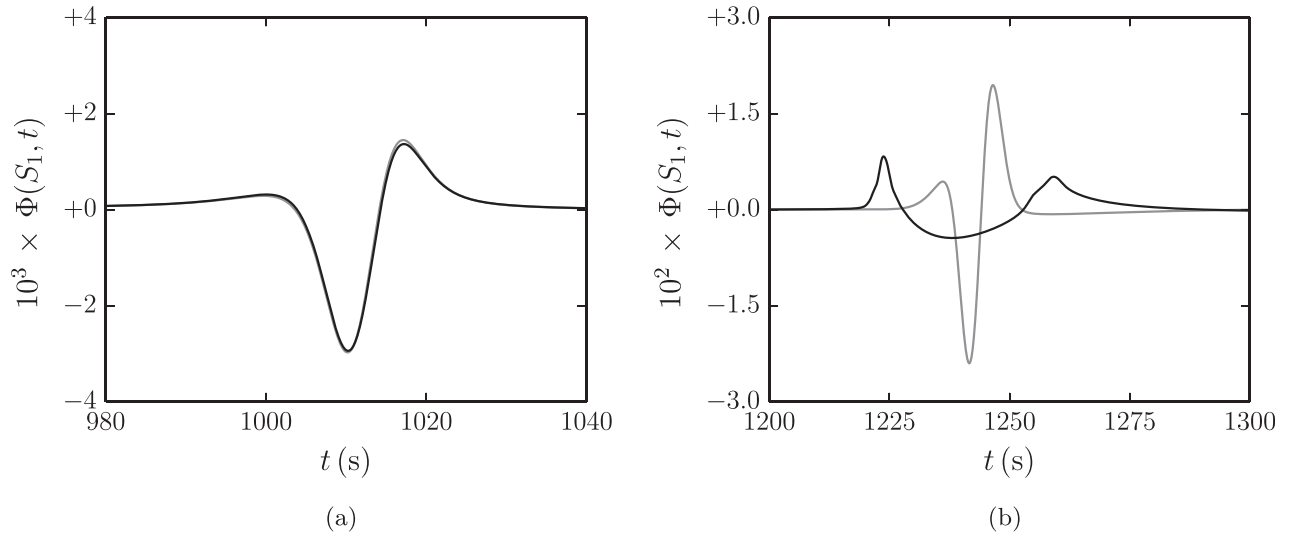


FIG. 14. NL case. Pressure  $\Phi$  recorded at the station  $S_1$ : (a) stratospheric arrival  $I_{s1}$ ; (b) thermospheric arrivals  $I_{tal} - I_{tbl}$ . The L case result is reported in gray.

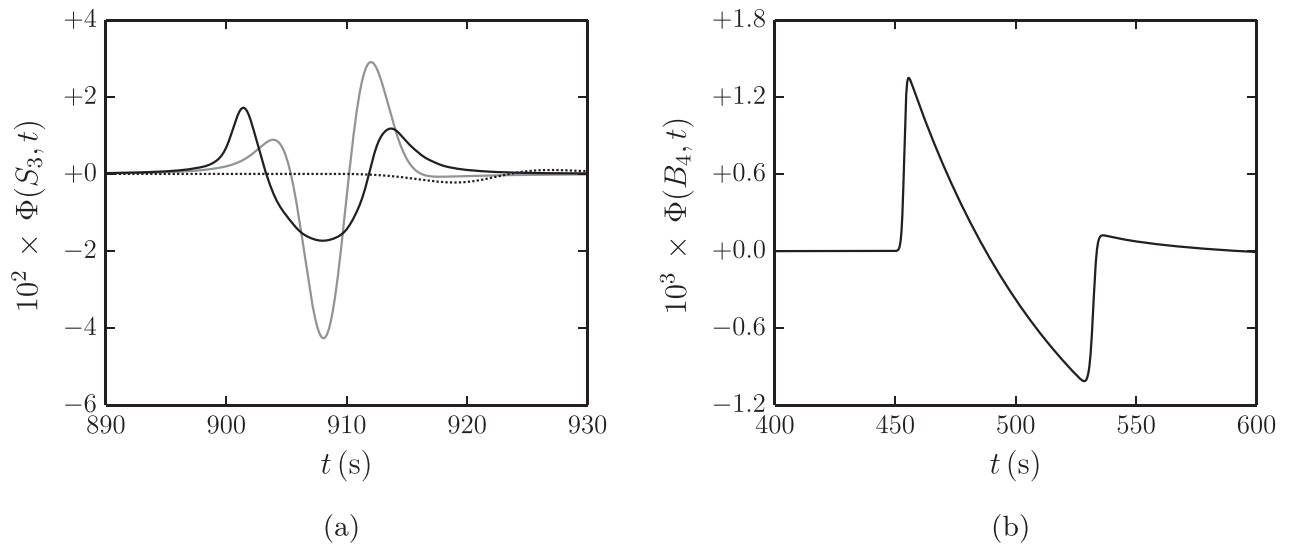


FIG. 15. NLW case. (a) Pressure  $\Phi$  recorded at the ground station  $S_3$ : result for the NLW case (black line), NL case (dotted line) and LW case (gray line). (b) Pressure  $\Phi$  recorded at the point  $B_4$ .

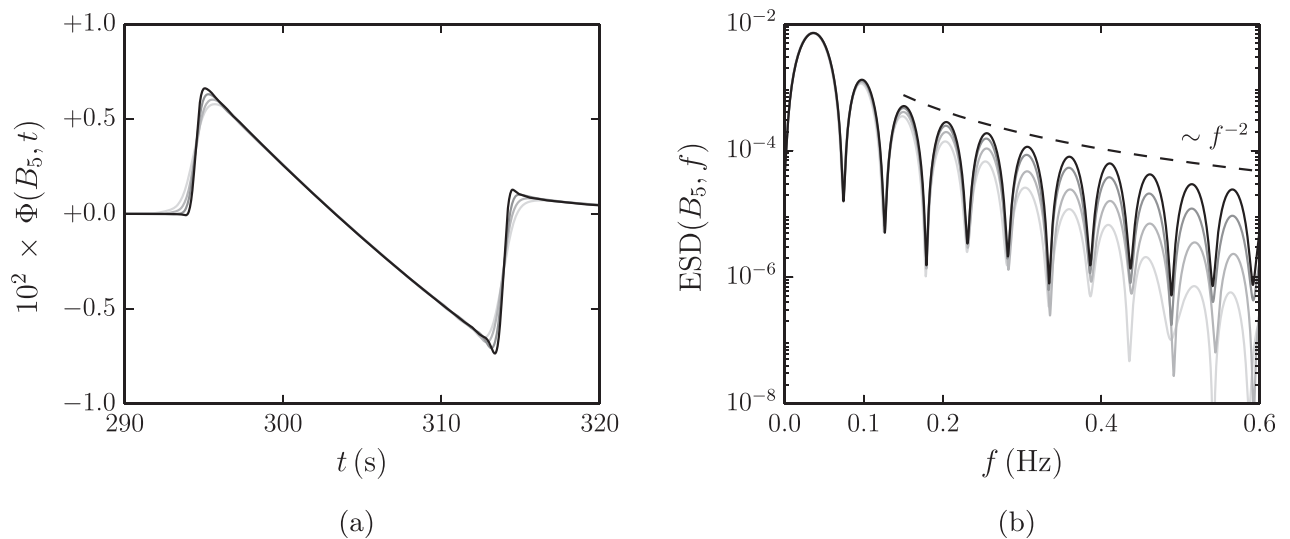


FIG. 16. Numerical accuracy. (a) Temporal signals and (b) corresponding one-sided energy spectral densities obtained at  $B_5$  with  $\alpha = 0.75$  (black line),  $\alpha = 1.0$  (slate gray line),  $\alpha = 1.25$  (gray line) and  $\alpha = 1.5$  (light gray line).

the thermosphere, most of the energy is contained in frequencies too low for significant attenuation to be observed below 180 km altitude [Fig. 15(b)]. The signal would have to propagate over far larger distances for viscous and thermal terms to affect the central part of the wave.

### Numerical accuracy

To illustrate the capability of the present algorithm, the signals recorded at the point  $B_5 = (0 \text{ km}, 90 \text{ km})$  using different grid spacings  $\alpha\Delta$ , with  $\alpha = 0.75, 1.0, 1.25, 1.5$ , are shown in Fig. 16(a). Because of the large source amplitude, a N-wave is observed at this location. The agreement between the different solutions is fairly good. In particular, the positions of the front and rear shocks seem to be well predicted even on the coarsest grid. The central part of the N-wave is also well resolved.

The energy spectral densities obtained with the four grid spacings are plotted in Fig. 16(b). The  $f^{-2}$ -behavior expected for the maxima of the spectrum of a balanced zero-mean N-wave is also reported in dashed line for comparison. Differences with respect to the ESD obtained on the finest grid appear at higher and higher frequencies as the mesh is refined. Convergence is observed for all grids on the first two lobes, which contain about 90% of the total energy of the signal, and despite appreciable attenuation with increasing frequency, the position of the maxima and minima is well reproduced even on the coarsest grid. Moreover, the relative error between the maxima of the energy spectral densities computed with  $\alpha = 0.75$  and  $\alpha = 1.0$  is lower than 50% up to the seventh harmonic, corresponding to a frequency of about 0.4 Hz. Finally, the relative error between the total energies obtained with  $\alpha = 0.75$  and  $\alpha = 1.0$  is around 2%.

## IV. CONCLUDING REMARKS

Long-range infrasound propagation is investigated in this work by performing direct numerical simulations of the two-dimensional Navier-Stokes equations. The aim is to highlight some specific physical features of infrasonic waves propagating in the Earth's atmosphere that are not properly captured by simplified modeling approaches. Four configurations with increasing source amplitudes are simulated. The refraction effects induced by temperature gradients are first illustrated, and the importance of thermoviscous dissipation during the linear propagation toward the upper atmosphere is clearly shown. The signature of different thermospheric signals is discussed with emphasis placed on the phase shift induced by a thermospheric caustic, and the behavior of the amplitude of ground level recordings as a function of the distance from the source is analyzed. An exponential-like decay of the amplitude is seen in the first shadow zone adjacent to the source, as also predicted by previous authors, whereas an overpressure up to 10% of the value at the source location can be observed beyond 300 km range. The influence of a wind profile on various phases is investigated in the second computation, and the effects of a stratospheric waveguide on the overpressure recorded at ground level are analyzed. A third

configuration, with a high source amplitude and in an atmosphere at rest, is investigated in order to examine the influence of non-linearities on the signature, amplitude and spectrum of thermospheric phases. The joint effects of wind and non-linearities are then illustrated in the last computation. In particular, it is shown that, for sufficiently large source energies, the signature of stratospheric phases can also be strongly affected. The roles of non-linearities and molecular dissipation during the propagation in the upper atmosphere, both of which are magnified by the decrease of the mean density with altitude, are also demonstrated, and it is found that, as a result of the low frequency generation associated with period lengthening, thermoviscous absorption effects can become less important for increasing source amplitudes.

The transfer functions of the numerical dissipation mechanisms in Fourier space are provided and it is shown that all the physical effects under study are correctly taken into account by the present numerical algorithm. A convergence analysis on a N-wave observed in the thermosphere in the last computation is reported as well, and an example of application of an improved and robust shock-capturing procedure is finally illustrated.

The numerical approach followed in this work is directly applicable to three-dimensional simulations of the Navier-Stokes equations for future work, which should allow insightful comparisons with measurements.

## ACKNOWLEDGMENTS

Present results have been obtained within the framework of Laboratoire Études et Modélisation Acoustique, a Contractual Research Laboratory shared between Commissariat à l'énergie et aux énergies alternatives, École Centrale de Lyon, C-Innov and Université Pierre et Marie Curie. This work was granted access to the High Performance Computing resources of the Très Grand Centre de calcul du CEA (TGCC) under the allocation 2015-200204 made by Grand Equipement National de Calcul Intensif. The first author thanks the Direction Générale de l'Armement for financial support and O. Gainville for discussions.

## APPENDIX A: ATMOSPHERIC PROFILES AND CONSTANTS

The speed of sound and wind profiles are defined by cubic splines, whose coefficients are reported in Table I. For a given altitude  $x_2 \in [x_{2,i}, x_{2,i+1}]$ , the value of  $\bar{f}$  at  $x_2$  is given by

$$\bar{f}(x_2) = a\bar{f}_i + b\bar{f}_{i+1} + \frac{1}{6} \left[ (a^3 - a)\bar{f}_i'' + (b^3 - b)\bar{f}_{i+1}'' \right] (x_{2,i+1} - x_{2,i})^2$$

where  $\bar{f} = \bar{c}$  or  $\bar{f} = \bar{u}_1$ . The two factors  $a$  and  $b$  are defined as

$$a = \frac{x_{2,i+1} - x_2}{x_{2,i+1} - x_{2,i}}, \quad b = 1 - a.$$

## APPENDIX B: SHOCK-CAPTURING METHODOLOGY

To handle the acoustic shocks generated during the propagation for sufficiently large source amplitudes, the shock-capturing technique proposed by Bogey *et al.*<sup>28</sup> is employed at each time step after the selective filtering procedure. It consists in adding artificial dissipation only where necessary, i.e., only near shock fronts, in such a way that smooth regions of the solution are not affected. The methodology involves two main steps. The locations of the discontinuities are first determined through a shock sensor. Then, a second-order filter is applied in conservative form with a strength  $\sigma^{\text{sc}}$  which is significant around the shocks but nil everywhere else. In the present work, the shock detector of Bogey *et al.*<sup>28</sup> is replaced by a new indicator, which is specifically developed for acoustic applications using the smoothness variables employed in the weighted essentially non-oscillatory schemes.<sup>31,32</sup> In a one-dimensional mesh, the following parameters  $\beta_k$ ,  $k = 0, 1, 2$ , are first calculated as

$$\begin{aligned}\beta_0 &= \frac{13}{12} (p'_{i-2} - 2p'_{i-1} + p'_i)^2 + \frac{1}{4} (p'_{i-2} - 4p'_{i-1} + 3p'_i)^2, \\ \beta_1 &= \frac{13}{12} (p'_{i-1} - 2p'_i + p'_{i+1})^2 + \frac{1}{4} (p'_{i-1} - p'_{i+1})^2, \\ \beta_2 &= \frac{13}{12} (p'_i - 2p'_{i+1} + p'_{i+2})^2 + \frac{1}{4} (3p'_i - 4p'_{i+1} + p'_{i+2})^2,\end{aligned}\quad (\text{B1})$$

where  $p'_i$  is the perturbation of pressure at node  $i$ . These indicators are combinations of centered and non-centered finite difference approximations of the first and second derivatives of  $p'$  and constitute an estimate of the regularity of the solution at point  $i$ . The coefficients  $\alpha_k$  and  $\omega_k$ ,  $k = 0, 1, 2$ , are then computed as

$$\alpha_k = \frac{1}{(\beta_k + \epsilon)^2}, \quad \omega_k = \frac{\alpha_k}{\sum_i \alpha_i}, \quad (\text{B2})$$

where  $\epsilon = 10^{-18}$  is a constant introduced to avoid divisions by zero. It is straightforward to show that, in smooth regions, the coefficients  $\beta_k$  are very small and the terms  $\omega_k$  tend to  $\frac{1}{3}$ .<sup>32</sup> The following sensor is thus introduced

$$r = \left( \sum_{k=0}^2 \left| \omega_k - \frac{1}{3} \right| \right)^2, \quad (\text{B3})$$

and the filtering strength  $\sigma_i^{\text{sc}}$  at the node  $i$  is calculated according to<sup>28</sup>

$$\sigma_i^{\text{sc}} = \frac{\sigma_{\text{max}}^{\text{sc}}}{2} \left( 1 - \frac{r_{\text{th}}}{r} + \left| 1 - \frac{r_{\text{th}}}{r} \right| \right), \quad (\text{B4})$$

where  $r_{\text{th}}$  is a threshold value equal to 0.8. The filtering magnitude  $\sigma_i^{\text{sc}}$  is thus nil away from shocks, where  $r < r_{\text{th}}$ , and takes increasing values up to  $\sigma_{\text{max}}^{\text{sc}} \in [0, 1]$  for increasing shock intensities. Finally, for the application of the conservative form of the shock-capturing filtering, the strengths  $\sigma_{i\pm 1/2}^{\text{sc}}$  [Eq. (24) in Bogey *et al.*<sup>28</sup>] are determined as the weighted averages

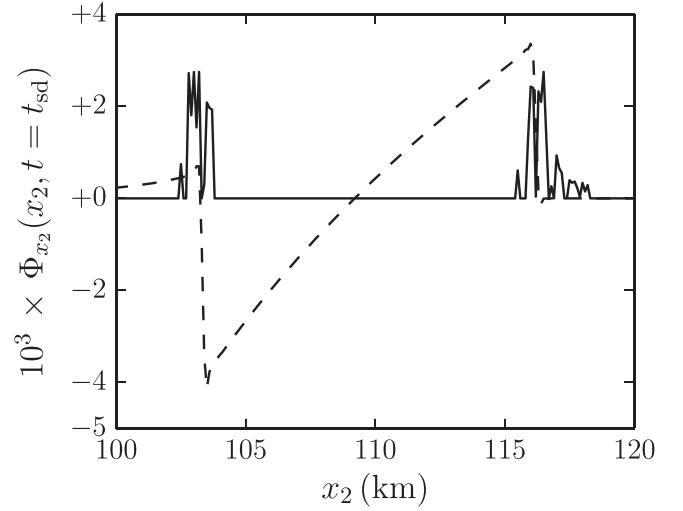


FIG. 17. Vertical cut  $\Phi_{x_2}(x_2, t_{\text{sd}})$  of the normalized pressure taken at  $t_{\text{sd}} = 366.7$  s (dashed line) and shock sensor  $\sigma^{\text{sc}}/50$  (solid line).

$$\begin{aligned}\sigma_{i-1/2}^{\text{sc}} &= \frac{1}{5} (2\sigma_{i-1}^{\text{sc}} + 2\sigma_i^{\text{sc}} + \sigma_{i+1}^{\text{sc}}), \\ \sigma_{i+1/2}^{\text{sc}} &= \frac{1}{5} (\sigma_{i-1}^{\text{sc}} + 2\sigma_i^{\text{sc}} + 2\sigma_{i+1}^{\text{sc}}).\end{aligned}\quad (\text{B5})$$

As an illustration, a vertical cut of the normalized pressure  $\Phi$  obtained in the NLW case,  $\Phi_{x_2}(x_2, t_{\text{sd}}) = \Phi(0 \text{ km}, x_2, t_{\text{sd}})$ , is shown in Fig. 17. The cut is taken at  $t_{\text{sd}} = 366.7$  s. The shock sensor  $\sigma^{\text{sc}}$  computed by performing the detection procedure along the  $x_2$  axis is also plotted. The highly dissipative second-order filter is applied only in two limited zones around the front and rear shocks, where  $\sigma^{\text{sc}}$  does not vanish, whereas the smooth central part of the N-wave is left unaffected.

<sup>1</sup>A. J. Bedard and T. M. Georges, “Atmospheric infrasound,” *Phys. Today* **53**(3), 32–37 (2000).

<sup>2</sup>A. Le Pichon, E. Blanc, and A. Hauchecorne, *Infrasound Monitoring for Atmospheric Studies* (Springer, Dordrecht, the Netherlands, 2010), Chaps. 2–3, pp. 29–118.

<sup>3</sup>A. Le Pichon, E. Blanc, D. Drob, S. Lambotte, J. X. Dessa, M. Lardy, P. Bani, and S. Vergnolle, “Infrasound monitoring of volcanoes to probe high-altitude winds,” *J. Geophys. Res.* **110**(D13), 1–12, doi:10.1029/2004JD0005587 (2005).

<sup>4</sup>J. Marty, D. Ponceau, and F. Dalaudier, “Using the international monitoring system infrasound network to study gravity waves,” *Geophys. Res. Lett.* **37**, L19802, doi:10.1029/2010GL044181 (2010).

<sup>5</sup>S. N. Kulichkov, I. P. Chunchuzov, G. A. Bush, and V. G. Perepelkin, “Physical modeling of long-range infrasonic propagation in the atmosphere,” *Iz. Atmos. Oceanic Phys.* **44**(2), 175–186 (2008).

<sup>6</sup>P. H. Rogers and J. H. Gardner, “Propagation of sonic booms in the thermosphere,” *J. Acoust. Soc. Am.* **67**(1), 78–91 (1980).

<sup>7</sup>O. Gainville, Ph. Blanc-Benon, and J. Scott, “Infrasound propagation in realistic atmosphere using nonlinear ray theory,” *AIP Conf. Proc.* **1474**(1), 343–346 (2012).

<sup>8</sup>J. B. Lonzaga, R. M. Waxler, J. D. Assink, and C. L. Talmadge, “Modelling waveforms of infrasound arrivals from impulsive sources using weakly nonlinear ray theory,” *Geophys. J. Int.* **200**(3), 1347–1361 (2015).

<sup>9</sup>L. C. Sutherland and H. E. Bass, “Atmospheric absorption in the atmosphere up to 160 km,” *J. Acoust. Soc. Am.* **115**(3), 1012–1032 (2004); “Erratum: ‘Atmospheric absorption in the atmosphere up to 1600 km,’” *J. Acoust. Soc. Am.* **120**(5), 2985 (2006).

- <sup>10</sup>A. D. Pierce, *Acoustics: An Introduction to its Physical Principles and Applications* (Acoustical Society of America, New York, 1985), Chaps. 8–11, pp. 371–615.
- <sup>11</sup>R. Marchiano, F. Coulouvrat, and J.-L. Thomas, “Nonlinear focusing of acoustic shock waves at a caustic cusp,” *J. Acoust. Soc. Am.* **117**(2), 566–577 (2005).
- <sup>12</sup>R. Waxler, L. G. Evers, J. Assink, and P. Blom, “The stratospheric arrival pair in infrasound propagation,” *J. Acoust. Soc. Am.* **137**(4), 1846–1856 (2015).
- <sup>13</sup>D. I. Blokhintsev, “Acoustics of a nonhomogeneous moving medium,” *Tech. Mem. 1399*, NACA (1956), Chaps. 1–2, pp. 1–66.
- <sup>14</sup>J. F. Lingeitch, M. D. Collins, and W. L. Siegmund, “Parabolic equations for gravity and acousto-gravity waves,” *J. Acoust. Soc. Am.* **105**(6), 3049–3056 (1999).
- <sup>15</sup>F. B. Jensen, W. Kuperman, M. Porter, and H. Schmidt, *Computational Ocean Acoustics* (Springer, New York, 2011), Chaps. 3–6, pp. 155–527.
- <sup>16</sup>M. S. Wochner, A. A. Atchley, and V. W. Sparrow, “Numerical simulation of finite amplitude wave propagation in air using a realistic atmospheric absorption model,” *J. Acoust. Soc. Am.* **118**(5), 2891–2898 (2005).
- <sup>17</sup>O. Marsden, L. Vayno, C. Bogey, and C. Bailly, “Study of long-range infrasound propagation with high-performance numerical schemes applied to the Euler equations,” in *Proceedings of the 13th Long Range Sound Propagation Symposium*, Lyon, France (2008), pp. 201–216.
- <sup>18</sup>C. de Groot-Hedlin, M. A. H. Hedlin, and K. Walker, “Finite difference synthesis of infrasound propagation through a windy, viscous atmosphere: Application to a bolide explosion detected by seismic networks,” *Geophys. J. Int.* **185**(1), 305–320 (2011).
- <sup>19</sup>R. Sabatini, O. Marsden, C. Bailly, and O. Gainville, “Numerical simulation of infrasound propagation in the Earth’s atmosphere: Study of a stratospheric arrival pair,” *AIP Conf. Proc.* **1685**(1), 090002 (2015).
- <sup>20</sup>S. Del Pino, B. Després, P. Havé, H. Jourden, and P. F. Piserchia, “3D finite volume simulation of acoustic waves in the Earth atmosphere,” *Comput. Fluids* **38**, 765–777 (2009).
- <sup>21</sup>C. de Groot-Hedlin, “Nonlinear synthesis of infrasound propagation through an inhomogeneous, absorbing atmosphere,” *J. Acoust. Soc. Am.* **132**(2), 646–656 (2012).
- <sup>22</sup>O. Marsden, C. Bogey, and C. Bailly, “A study of infrasound propagation based on high-order finite difference solutions of the Navier-Stokes equations,” *J. Acoust. Soc. Am.* **135**(3), 1083–1095 (2014).
- <sup>23</sup>O. Marsden, C. Bogey, and C. Bailly, “Direct noise computation of the turbulent flow around a zero-incidence airfoil,” *AIAA J.* **46**(4), 874–883 (2008).
- <sup>24</sup>C. Bogey, O. Marsden, and C. Bailly, “Large-eddy simulation of the flow and acoustic fields of a reynolds number  $10^5$  subsonic jet with tripped exit boundary layers,” *Phys. Fluids* **23**(3), 035104 (2011).
- <sup>25</sup>O. Marsden, C. Bogey, and C. Bailly, “Investigation of flow features around shallow round cavities subject to subsonic grazing flow,” *Phys. Fluids* **24**(12), 125107 (2012).
- <sup>26</sup>C. Bogey and C. Bailly, “A family of low dispersive and low dissipative explicit schemes for noise computations,” *J. Comput. Phys.* **194**(1), 194–214 (2004).
- <sup>27</sup>J. Berland, C. Bogey, O. Marsden, and C. Bailly, “High-order, low dispersive and low dissipative explicit schemes for multiple-scale and boundary problems,” *J. Comput. Phys.* **224**, 637–662 (2007).
- <sup>28</sup>C. Bogey, N. De Cacqueray, and C. Bailly, “A shock-capturing methodology based on adaptive spatial filtering for high-order nonlinear computations,” *J. Comput. Phys.* **228**, 1447–1465 (2009).
- <sup>29</sup>O. Gainville, Ph. Blanc-Benon, E. Blanc, R. Roche, C. Millet, F. Le Piver, B. Despres, and P. F. Piserchia, “Misty picture: A unique experiment for the interpretation of the infrasound propagation from large explosive sources,” in *Infrasound Monitoring for Atmospheric Studies* (Springer, Dordrecht, the Netherlands, 2010), Chap. 18, pp. 575–598.
- <sup>30</sup>O. Marsden and O. Gainville, “Nonlinear effects in infrasound propagation simulations,” in *Proceedings of the Acoustics 2012 Nantes Conference*, Nantes, France, 23–27 April 2012, pp. 4031–4036.
- <sup>31</sup>G.-S. Jiang and C.-W. Shu, “Efficient implementation of weighted ENO schemes,” *J. Comput. Phys.* **126**, 202–228 (1996).
- <sup>32</sup>R. Borges, M. Carmona, B. Costa, and W. S. Don, “An improved weighted essentially non-oscillatory scheme for hyperbolic conservation laws,” *J. Comput. Phys.* **227**, 3191–3211 (2008).
- <sup>33</sup>C. K. W. Tam and Z. Dong, “Radiation and outflow boundary conditions for direct computation of acoustic and flow disturbances in a nonuniform mean flow,” *J. Comp. Acoust.* **04**(2), 175–201 (1996).
- <sup>34</sup>D. J. Bodony, “Analysis of sponge zones for computational fluid mechanics,” *J. Comput. Phys.* **212**(2), 681–702 (2006).
- <sup>35</sup>C. Bogey and C. Bailly, “Turbulence and energy budget in a self-preserving round jet: Direct evaluation using large-eddy simulation,” *J. Fluid Mech.* **627**, 129–160 (2009).
- <sup>36</sup>P. G. Bergmann, “The wave equation in a medium with a variable index of refraction,” *J. Acoust. Soc. Am.* **17**(4), 329–333 (1946).
- <sup>37</sup>F. Coulouvrat, “Théorie géométrique non linéaire de la diffraction en zone d’ombre” (“Nonlinear geometrical theory of diffraction in the shadow zone”) *C. R. Acad. Sci. Paris.* **325**, 69–75 (1997).
- <sup>38</sup>G. Hanique-Cockenpot, “Étude numérique de la propagation non linéaire des infrasons dans l’atmosphère” (“A numerical study of nonlinear infrasound propagation in atmosphere”), Ph.D. thesis, Ecole Centrale de Lyon, France (2011), No. 2011-32.
- <sup>39</sup>R. O. Cleveland, “Propagation of sonic booms through a real, stratified atmosphere,” Ph.D. dissertation, The University of Texas at Austin, TX 1995.
- <sup>40</sup>S. N. Kulichkov, “Evidence for nonlinear atmospheric effects in infrasound propagation from explosions of different types and yields,” in *Nonlinear Acoustics - Fundamentals and Applications: 18th International Symposium on Nonlinear Acoustics - ISNA 18*, edited by B. O. Enflo, C. M. Hedberg, and L. Kari (AIP, New York, 2008), pp. 401–404.